Wetting, budding, and fusion—morphological transitions of soft surfaces



2005 J. Phys.: Condens. Matter 17 S2885

(http://iopscience.iop.org/0953-8984/17/31/016)

INSTITUTE OF PHYSICS PUBLISHING JOURNAL OF PHYSICS: CONDENSED MATTER

J. Phys.: Condens. Matter **17** (2005) S2885–S2902 doi:10.1088/0953-8984/17/31/016

# Wetting, budding, and fusion—morphological transitions of soft surfaces

**Reinhard Lipowsky, Martin Brinkmann, Rumiana Dimova, Chris Haluska, Jan Kierfeld and Julian Shillcock**

Max Planck Institute of Colloids and Interfaces, 14424 Potsdam, Germany[1]

Received 28 March 2005
Published 22 July 2005
Online at stacks.iop.org/JPhysCM/17/S2885

**Abstract**

Biomimetic systems typically contain soft surfaces such as fluid interfaces or bilayer membranes that attain a large variety of different shapes and undergo morphological transitions between those shapes. This article briefly reviews several different examples from a unified perspective: liquids at chemically patterned and/or topographically structured surfaces; the formation of membrane buds from membrane domains; and the fusion of bilayer membranes and vesicles.

(Some figures in this article are in colour only in the electronic version)

## 1. Introduction and overview

Biomimetic systems typically contain soft surfaces such as fluid interfaces or membranes. These latter surfaces attain a large variety of shapes, undergo morphological transitions between those shapes, are susceptible to weak forces, and, in general, provide soft scaffolds for more complex architectures.

The present article briefly reviews recent work on morphological transitions in such systems. We will use a top down approach and start from the simplest system, a small droplet of liquid such as water that is deposited on a solid substrate. If this substrate is chemically uniform and planar, the droplet attains the unique shape of a spherical cap. In contrast, a variety of different shapes and morphological transitions are found if the substrate is chemically patterned [1–12] or topographically structured [13]. The basic mechanism underlying this polymorphism is the *freedom* of contact angles at *pinned* contact lines as emphasized below.

Several experimental methods such as electrowetting [14–17, 13] and employing switchable monolayers of grafted molecules, which can attain several metastable conformations [18–22], have been developed in order to rapidly change the contact angle of the underlying substrate. In principle, any of these methods can be used in order to drive

[1] http://www.mpikg.mpg.de/th/

  

the system through a morphological wetting transition and to switch the liquid morphology in a controlled manner.

So far, morphological wetting transitions have been experimentally observed in the millimetre and micrometre regime but should also occur in the nanometre regime. For substrate domains or topographies with a linear dimension below about 100 nm, these transitions should be affected by the line tension of the contact lines [23–25]. Other aspects of wetting that we have recently studied include a general stability analysis of liquid morphologies [26, 27], liquid bridges across slit pores [28–30], and nucleation at circular surface domains [31].

The second type of soft surface that we will consider is provided by *bilayer membranes* composed of amphiphilic molecules such as lipids or diblock copolymers. These molecular bilayers can be stretched by external constraints or forces and exhibit different tension regimes. In the *high* tension regime below the tension of rupture, closed membranes or vesicles behave much like liquid droplets. This regime is particularly interesting if the vesicles adhere to chemically patterned substrates [32, 33]. In the *low* tension regime, membranes and vesicles undergo new kinds of shape transformations not found for liquids. One particularly interesting example is provided by budding, i.e., by the expulsion of small, spherical buds from larger vesicles.

More than ten years ago, we theoretically predicted a robust and generic mechanism for the formation of such membrane buds from intramembrane domains [34–37]. This mechanism is governed by the line tension of the domain boundaries and modulated by the spontaneous curvature of the membrane domains. Recently, this process of domain-induced budding has been experimentally confirmed by fluorescence microscopy of giant vesicles that have a diameter of many micrometres [38]. The membranes of these vesicles were composed of the phospholipid DOPC, cholesterol, and sphingomyelin corresponding to the 'raft' mixture that has been postulated to lead to lipid domains in biomembranes [39–41].

The experiments in [38] provide direct evidence for the line tension of intramembrane domains [34, 35] even on the micrometre scale and are consistent with previous observations of giant vesicles that revealed domain formation [42] and budding [43] for membranes with the same lipid composition. Domain-induced budding of giant vesicles has presumably been seen for many other kinds of multi-component membranes [44–48] even though the detection of the underlying membrane domains remains an experimental challenge. The same process also occurs for smaller vesicles that have a diameter of 20–200 nm as observed in computer simulations [49–52].

Budding involves the formation of a small membrane neck that connects the bud with the larger vesicle. There is a rather different process, the fusion of two separate membranes, that leads to the formation of the same neck-like membrane structure, now representing the so-called fusion pore.

Membrane fusion is a ubiquitous process of life. A prominent example is provided by the fusion of synaptic vesicles to the outer membranes of nerve cells. In spite of its ubiquity, the basic mechanisms underlying the process of membrane fusion are still poorly understood. We have recently gained new insight into this process by computer simulations on small vesicles with a diameter of 30 nm [53] and micropipette experiments on giant vesicles with a diameter of tens of micrometres [54]. These studies show that vesicle fusion is a *multiscale* process that involves a wide range of length and timescales.

This article is organized as follows. Liquids at solid substrates are discussed in section 2 which starts with an elementary description of the interrelation of pinned contact lines and free contact angles and then describes a few examples for liquid morphologies and morphological transitions at chemically patterned and topographically structured substrates. Bilayer membranes and vesicles are considered in section 3; the first subsection gives an update

on the process of domain-induced budding; the second subsection describes our recent attempts to understand membrane fusion via computer simulations and optical microscopy.

## 2. Liquids at structured surfaces

Let us consider the general situation of a rigid surface that represents the boundary between a fluid phase $\alpha$ and a solid substrate $\sigma$. We now place a small amount of liquid $\beta$ at this surface, i.e., in the $\alpha\sigma$ interface. This liquid droplet is bounded by the solid surface and by the interface between the two fluid phases $\alpha$ and $\beta$. The latter interface attains a shape of *constant mean curvature* as determined by the balance of Laplace pressure and interfacial tension.

When the liquid is deposited on a homogeneous substrate, the contact zone of liquid and substrate is characterized by movable contact lines and fixed contact angle. The latter angle is determined by the classical Young equation if one can ignore the effects of line tension. In contrast, if the liquid is placed on a chemically patterned or topographically structured substrate surface, their contact zone is characterized by pinned contact lines and free contact angles. As a result of this latter freedom, one obtains *morphological wetting transitions* between different constant mean curvature shapes [1–3, 13].

In the following subsections, we will discuss a few relatively simple examples. First, we will focus on surfaces that contain two kinds of surface domains, which attract and repel the liquid, respectively. These domains can have many different shapes. We will discuss only two cases, circular and striped domains. Second, we will consider a rather simple surface topography provided by surface channels or grooves with a rectangular cross section. In each case, one encounters a variety of liquid morphologies and morphological transitions for which one can derive a complete classification.

### 2.1. Pinned contact lines and free contact angles

*2.1.1. Contact line pinning by surface domains.* In order to illustrate the freedom of contact angles at pinned contact lines, let us first consider circular surface domains, $\gamma$, which are embedded in a chemically distinct substrate surface, $\delta$. The $\gamma$ domains are taken to be hydrophilic (in general: lyophilic), the $\delta$ surface is taken to be hydrophobic (in general: lyophobic). When we place a droplet of water, $\beta$, on top of such a circular domain, the liquid attains the shape of a spherical cap with contact angle $\theta = \theta_\gamma$; see figure 1; regime (I). As we add more liquid to this droplet, it grows until it covers the whole $\gamma$ domain. At this point, the contact line sits on top of the $(\gamma\delta)$ domain boundary. If we continue to add liquid as in figure 1, we enter regime (II): the position of the contact line remains fixed *while the contact angle grows until it reaches the limiting value* $\theta = \theta_\delta$. Beyond this point, the contact line becomes depinned from the $(\gamma\delta)$ domain boundary and the droplet starts to spread onto the lyophobic $\delta$ domain where it attains the contact angle $\theta_\delta$ [1].

Similar behaviour is found for surface domains of any shape. In particular, along any contact line segment (CLS), which is pinned to a $(\gamma\delta)$ surface domain boundary, the contact angle $\theta = \theta_\mathrm{p}$ is free to vary over the whole range [1]

$$\theta_\gamma \leqslant \theta_\mathrm{p} \leqslant \theta_\delta \qquad \text{(CLS pinned to domain boundary).} \tag{1}$$

*2.1.2. Contact line pinning by surface topographies.* Next, consider a substrate that is chemically homogeneous with contact angle $\theta$ but has a nonplanar surface topography. Simple examples for such topographically structured surfaces, which can be fabricated in the micrometre regime by standard photolithographic methods, are provided by surface channels

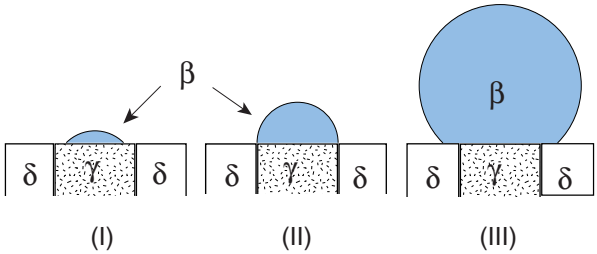


**Figure 1.** Side view of water droplet $\beta$ (dark) on a circular hydrophilic $\gamma$ domain (white with confetti) in a hydrophobic $\delta$ substrate (white): (I) for small volume, the droplet forms a spherical cap with contact angle $\theta = \theta_\gamma$; (III) for large volume, the droplet forms a spherical cap with $\theta = \theta_\delta$; and (II) for intermediate volumes, the contact angle of the spherical cap depends on the volume and is free to vary over the range $\theta_\gamma < \theta = \theta_p < \theta_\delta$ [1].

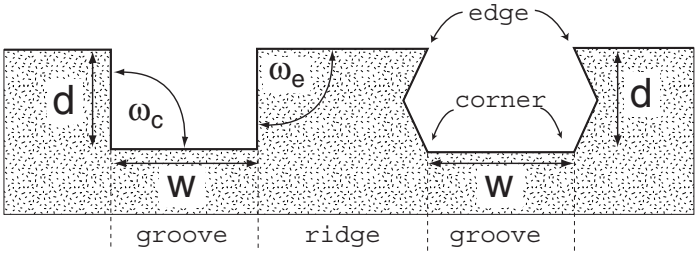


**Figure 2.** Side view of two surface channels or grooves separated by ridges. Both grooves have depth $d$ and width $w$. The opening angle of the groove corner is denoted by $\omega_c$, the opening angle of the groove edge by $\omega_e$. For the rectangular cross section on the left, both opening angles are identical and equal to $\pi/2$; for the hexagonal cross section on the right, one has $\omega_c = 2\pi/3$ and $\omega_e = \pi/3$.

or grooves with a certain cross section; see figure 2. As indicated in this figure, each cross section can be characterized by the opening angle $\omega_e$ of the upper groove edge: for a rectangular and a hexagonal cross section, this angle is equal to $\omega_e = \pi/2$ and $\pi/3$, respectively.

If one deposits some liquid in these surface grooves, the contact angle attains the fixed value $\theta = \theta_\gamma$ along all contact line segments that are located within the groove bottoms, groove sidewalls, or ridges between the grooves. However, many wetting morphologies involve contact line segments that are pinned along the upper groove edges as indicated in figure 3. For such a pinned contact line segment (CLS), the contact angle $\theta = \theta_p$ is free to vary over the range [13]

$$\theta \leqslant \theta_p \leqslant \theta + \pi - \omega_e \qquad \text{(CLS pinned to groove edge)}. \tag{2}$$

### *2.2. Liquid morphologies governed by surface domains*

Many experimental methods have been developed by which one can design chemically structured substrates with a variety of hydrophilic and hydrophobic (in general: lyophilic and lyophobic) surface domains. The linear size of these surface domains can be varied over a wide range of length scales from the millimetre down to the nanometre regime [2, 4–8, 12, 9–11].

*2.2.1. Optimized contacts.* The simplest domain geometry is provided by a single circular domain as discussed before; see figure 1. This case is, however, exceptional since a droplet

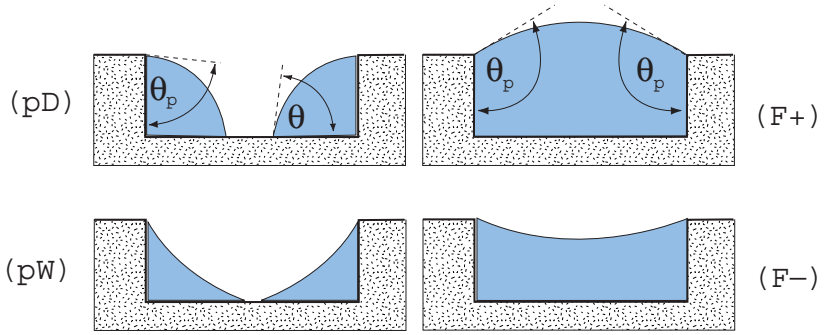


**Figure 3.** Side view of liquid morphologies (dark) on a single surface channel or groove (white with confetti) with rectangular cross section. The morphologies (pD) and (pW) represent localized droplets and thin extended wedges, respectively, both of which are pinned to the upper groove edges. The morphologies (F+) and (F−) represent extended liquid filaments with positive and negative Laplace pressure. For contact line segments at the groove bottom, groove sidewalls, and ridges, the contact angle attains the fixed value $\theta$ of the substrate material. For contact line segments that are pinned to the upper groove edges, the contact angle $\theta_p$ is free to vary over the range $\theta < \theta_p < \theta + \pi/2$ and its value is determined by the liquid volume.

of $\beta$ liquid can still attain the shape of a spherical cap even in the presence of the surface domain. In the limit of large liquid volume $V_\beta$, this cap approaches a complete sphere which is the shape with the smallest surface area of the $(\alpha\beta)$ interface. Therefore, the droplet can simultaneously *maximize* its contact area with the hydrophilic $\gamma$ domain and *minimize* the area of its $(\alpha\beta)$ interface.

The behaviour becomes more interesting if one has (i) a single $\gamma$ domain with a sufficiently anisotropic shape, (ii) a single $\gamma$ domain which is multiply connected, or (iii) a pattern consisting of several disconnected $\gamma$ domains. In all of these cases, the droplet tries to maximize its contact with the $\gamma$ domains and to avoid the $\delta$ domains but it can only do so if its $(\alpha\beta)$ interface deviates from a spherical segment. If the droplet is large compared to the size of the surface domain patterning, the interfacial region close to the contact line develops pronounced folds [24, 55, 56]. On the other hand, if the droplet size is initially comparable to the size of the $\gamma$ domain, the droplet first adapts to the $\gamma$ domain for small volumes but then undergoes a morphological wetting transition to a more spherical shape at large volumes [1, 2, 6, 8, 3, 12].

*2.2.2. Striped surface domains.* A relatively simple example for noncircular $\gamma$ domains is provided by long rectangular stripes as in figures 4(a)–(d). Now, let us deposit a certain amount of $\beta$ liquid onto such a stripe. For sufficiently small volume $V_\beta$, the liquid forms a small spherical cap bounded by a circular contact line with contact angle $\theta = \theta_\gamma$. This spherical cap grows as we increase the liquid volume until the contact line touches the $(\gamma\delta)$ domain boundary; see figure 4(a). If the volume is increased beyond this point, the evolution of the droplet shape depends strongly on the value of the contact angle $\theta_\gamma$.

In fact, the contact angle $\theta_\gamma$ on the lyophilic stripe exhibits the boundary value [3]

$$\theta_{\mathrm{fi}}^{\infty} = \arccos(\pi/4) \simeq 38^\circ \tag{3}$$

which separates two different wetting regimes[2]. These two regimes are characterized by qualitatively different behaviour as one deposits an increasing amount of liquid onto the stripe.

[2] The subscript 'fi' and the superscript $\infty$ indicate that this is the contact angle of a liquid filament in the limit of large volumes. In [3], $\theta_{\mathrm{fi}}$ was denoted by $\theta_{\mathrm{ch}}$ since the filaments were called channels.

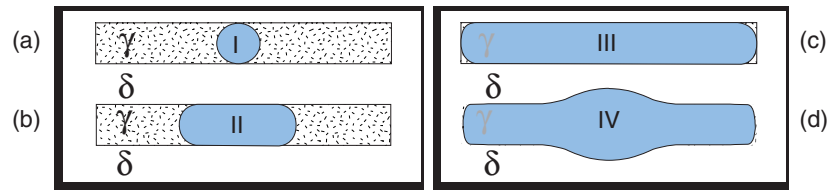


**Figure 4.** Top view of liquid morphologies (dark) on surface domains $\gamma$ (white with confetti) within a hydrophobic substrate $\delta$ (white). The $\gamma$ domains have the shape of a long, rectangular stripe; the corresponding contact angle $\theta_\gamma$ is smaller than the boundary value as given by (3). With increasing volume, the liquid droplet attains the four states I–IV: (a) for relatively small volumes, the droplet has the shape of a spherical cap I with a contact line which eventually touches the $\gamma\delta$ domain boundary; (b) as the volume is further increased, an extended filament II is formed which has freely moving end caps; (c) the filament III covers the $\gamma$ stripe completely and, thus, has fixed end caps; (d) as one adds even more liquid volume, the droplet undergoes a morphological transition to the filament state IV with a single bulge.

If the stripe has contact angle $\theta_\gamma < \theta_{\rm fi}^\infty$, the wetting layer forms a liquid filament (or channel) which becomes longer and longer as one deposits more and more liquid. For $\theta_\gamma > \theta_{\rm fi}^\infty$, on the other hand, such a long filament cannot be attained but only a short one which transforms into a localized droplet. In other words, it is easy to 'paint' long $\gamma$ stripes provided $\theta_\gamma < \theta_{\rm fi}^\infty$ but it is *impossible* to do so for $\theta_\gamma > \theta_{\rm fi}^\infty$. In the limit of large stripe length, this distinction can be described by a global morphology diagram with a line of discontinuous transitions that ends in a critical point [3].

The shape evolution shown in figure 4 corresponds to a $\gamma$ stripe of finite length with a contact angle $\theta_\gamma$ that satisfies $\theta_\gamma \ll \theta_{\rm fi}^\infty$. In this case, the growing droplet in figure 4(a) transforms into an extended filament which partially covers the striped surface domain; see figure 4(b). Inspection of this figure shows that the contact line of such a filament, which is shorter than the striped domain, consists of two distinct kinds of segments:

(i) Those contact line segments that are pinned along the $(\gamma\delta)$ domain boundary of the underlying surface stripe. Along those domain boundaries, the contact angle $\theta = \theta_{\rm p}$ is not fixed but satisfies the inequality $\theta_\gamma < \theta_{\rm p} < \theta_\delta$ as in (1); and
(ii) The two short *transverse* segments of the contact line which bound the two end caps of the filament. Since these latter segments lie within the $\gamma$ surface domain, the corresponding contact angle has the fixed value $\theta = \theta_\gamma$.

Now, as we continue to add liquid, the filament continues to grow until it covers the stripe completely as shown in figure 4(c). At this point, the transverse contact line segments at the two end caps of the filament become pinned to the $\gamma\delta$ domain boundary as well. Thus, as soon as the filament covers the stripe completely, the contact angle at the two end caps is no longer fixed but can now also vary within the whole range $\theta_\gamma < \theta_{\rm p} < \theta_\delta$ as given by (1). As we add even more liquid, the contact angles along the pinned contact line continue to grow until the filament becomes unstable and develops a single bulge as shown in figure 4(d). This latter morphological wetting transition was first studied, both experimentally and theoretically, in [2].

### *2.3. Liquid morphologies governed by surface topography*

*2.3.1. Surface grooves with rectangular cross section.* Regular surface topographies such as channels or grooves can be fabricated using standard photolithography. A rather simple example is provided by surface grooves with rectangular cross section; see figure 2. We have recently obtained a complete classification of the liquid morphologies formed in such grooves

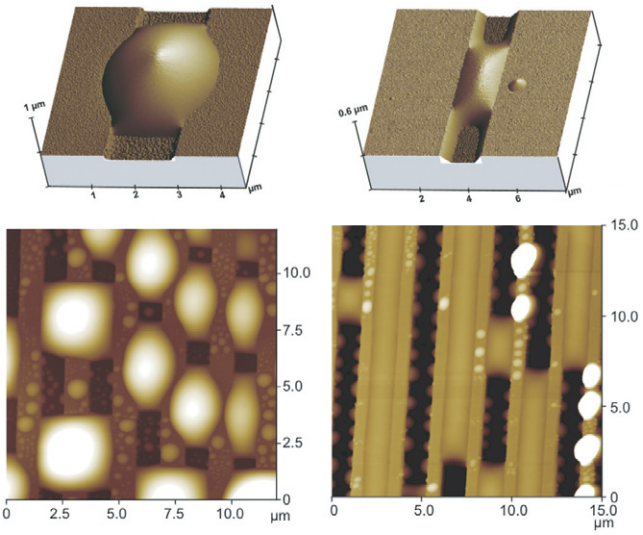


**Figure 5.** Atomic (or scanning) force microscopy images of liquid morphologies on silicon substrates with rectangular surface channels or grooves which have a width of about one micrometre. On the left, the liquid does not enter the grooves but forms large lemon-shaped droplets overlying the grooves (dark stripes). On the right, the liquid enters the grooves and forms extended filaments separated by essentially empty groove segments (dark stripes). In the bottom row, one sees several parallel surface grooves in both images; in the top row, there is only one such groove with a single droplet (left) or filament (right). Close inspection of the upper right image reveals (i) that this filament is connected to thin wedges along the lower groove corners and (ii) that the contact line bounding the meniscus of the filament is pinned to the upper groove edges [13].

which include localized droplets, extended filaments, and thin wedges at the lower groove corners [13]. Examples for these morphologies as observed by atomic (or scanning) force microscopy (AFM) are shown in figure 5.

The theoretical classification described in [13] is based (i) on general considerations such as the relation given by (2), (ii) on analytical shape calculations which are feasible for relatively simple morphologies such as liquid filaments with constant cross section, see figure 6, and (iii) on numerical minimization of the liquid free energy which leads to constant mean curvature surfaces. One useful prediction of our theory is that the experimentally observed polymorphism of the wetting liquid depends only on two parameters: (i) the aspect ratio $X \equiv d/w$ of the groove geometry, i.e., the ratio of the groove depth $d$ to the groove width $w$; and (ii) the contact angle $\theta_\gamma$ which characterizes the homogeneous substrate material. As a result one obtains the morphology diagram in figure 7.

*2.3.2. Applications to microfluidics.* Inspection of figure 7 shows that one has to distinguish seven different liquid morphologies which involve localized droplets (D), extended filaments (F), and thin wedges (W) at the lower groove corners. For microfluidics applications, the most important morphology regime is ($F^-$) which corresponds to stable filaments. Since this regime covers a relatively small region of the morphology diagram, see figure 7, it can only be obtained if one carefully matches the groove geometry described by its aspect ratio $X$ with the substrate wettability as described by the contact angle $\theta$.

The morphology regime ($F^-$) corresponds to extended liquid filaments for which the surface grooves or channels act as confining microcompartments. These filaments have the

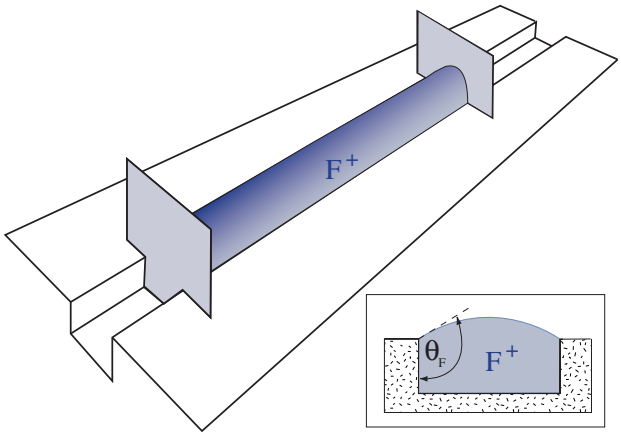


**Figure 6.** Liquid filament ($F^+$) with positive Laplace pressure, i.e., with a meniscus that is curved away from the substrate. The filament is located within the rectangular surface groove and is 'sandwiched' between two pistons. In mechanical equilibrium, the total force exerted by the filament onto each piston wall must vanish. The inset shows the filament cross section and the associated filament angle $\theta_p = \theta_F$ which is uniquely determined by the aspect ratio $X$ of the surface groove and the contact angle $\theta$ of the substrate [13].

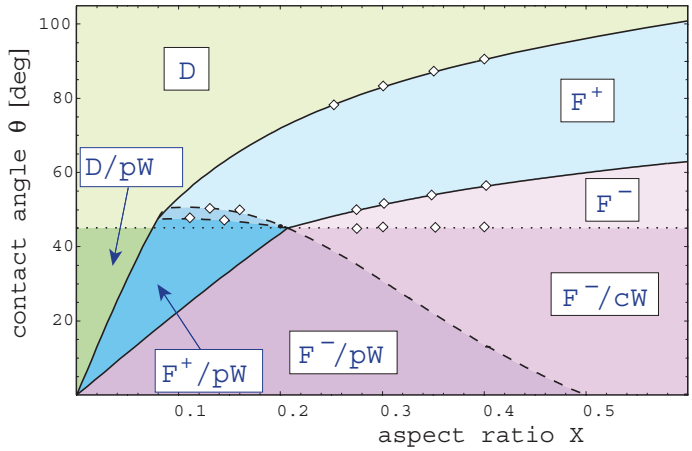


**Figure 7.** Morphology diagram as a function of the aspect ratio $X$ of the surface groove, defined by the ratio of groove depth to groove width, and the contact angle $\theta$ which characterizes the interaction between substrate material and liquid. This diagram contains seven different morphology regimes which involve localized droplets (D), extended filaments (F), and thin wedges (W) in the lower groove corners. The wedges (pW) contain contact line segments that are pinned to the upper groove edges whereas the wedges (cW) contain no such segments. The filaments (F+) and (F−) have positive and negative Laplace pressure, respectively. The diagram represents a complete classification of all possible wetting morphologies and should apply to all liquids and substrate materials [13].

remarkable property that they grow and shrink in length while their cross section stays the same when more liquid is added; compare figure 6. In addition, the filaments in the morphology regime ($F^-$) have a well-defined length since they are not connected to any wedges in the lower groove corners. The minus sign indicates that these filaments have a negative Laplace pressure which implies that their meniscus is curved downwards towards the substrate. In the

microregime and nanoregime, such filaments can tolerate a relatively large overpressure, the size of which increases with decreasing channel width. Thus, a water filament in a narrow channel that has a width of 100 nm can sustain an overpressure of 15 atm. In contrast, if the channel had a width of one millimetre, the water filament could only sustain a thousandth part of an atmosphere.

One direct application of the overall morphology diagram is obtained if one combines the surface topography studied here with methods to *switch* the contact angle. One such method is provided by electrowetting [14–17]; alternative methods are based on substrate surfaces with grafted molecules which exhibit several metastable conformations and can be switched by light [18, 19, 21], temperature [20], or electric potential [22]. Let us consider, for example, a short filament (F+) with positive Laplace pressure which is in mechanical equilibrium with a reservoir such as a large droplet. If we now decrease the contact angle in the groove in such a way that we enter the filament regime (F−) with negative Laplace pressure, the filament imbibes liquid from the large droplet and advances into the groove; a reversible realization of such a process has been demonstrated by electrowetting [13].

## 3. Bilayer membranes and vesicles

Bilayer membranes are composed of amphiphilic molecules such as lipids or diblock copolymers which have an overall rod-like shape with a typical length of 2 nm and a cross sectional area of about 1 $\mathrm{nm}^2$. These membranes form closed vesicles that can have a linear size of up to 50 $\mu$m and an area of up to $10^{10}$ $\mathrm{nm}^2$. Thus, bilayer membranes involve a wide range of length scales. In addition, these membranes exhibit a unique combination of robustness and flexibility to mechanical perturbations.

Bilayer membranes can be stretched by external constraints and forces and exhibit several distinct tension regimes. Consider a membrane segment with area $\mathcal{A}$ and bending rigidity $\kappa$, which is typically of the order of $10^{-19}$ J for lipid bilayers. One can then define two intrinsic tension scales: the size-dependent 'bending tension', $\Sigma_{\mathcal{A}} \equiv \kappa/\mathcal{A}$, which is of the order of $10^{-6}$ mJ $\mathrm{m}^{-2}$ for a membrane segment with a linear size of 10 $\mu$m, and the tension of rupture, $\Sigma_{\mathrm{rup}}$, which is typically of the order of 5–10 mJ $\mathrm{m}^{-2}$. If the tension exceeds the tension of rupture $\Sigma_{\mathrm{rup}}$, it perforates the membrane which then attains a new state of lower tension.

In addition, one may use a practical tension scale that depends on the resolution of the microscopy method. Thus, assume that the smallest objects that we can resolve has a linear dimension $L$. We can then define another tension scale $\Sigma_L \equiv \kappa/L^2$. For an optical microscope, one typically has $L = 250$ $\mu$m which implies $\Sigma_L \simeq 10^{-3}$ mJ $\mathrm{m}^{-2}$. In the following, we will define the low tension and high tension regime by $\Sigma_{\mathcal{A}} < \Sigma < \Sigma_L$ and $\Sigma_L < \Sigma < \Sigma_{\mathrm{rup}}$, respectively.

In the high tension regime, the shapes of fluid membranes look very similar to those of fluid interfaces and are again characterized by *constant mean curvature*. Thus, closed membranes or vesicles that are deposited on adhesive substrates behave much like the liquid droplets discussed in the previous section [32, 33]. The main difference to liquid shapes is that the vesicle shapes in the high tension regime exhibit effective contact angles [57] that are *always* determined by the vesicle geometry [33].

In the low tension regime, on the other hand, the shapes of vesicles are primarily governed by bending and curvature. This leads to new morphological transitions that are not accessible to liquid droplets. One particularly intriguing example is budding, i.e., the expulsion of a smaller spherical bud from a larger 'mother' vesicle. The bud and the 'mother' vesicle are still connected by a small membrane neck that resembles a catenoidal segment and is characterized by essentially zero mean curvature.

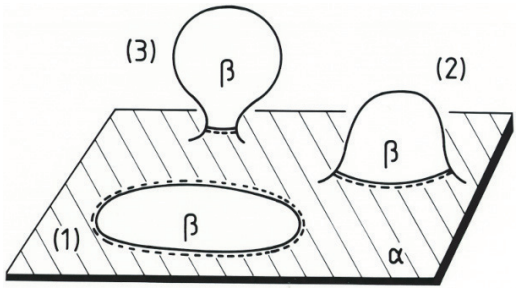


**Figure 8.** A fluid domain ($\beta$) in a fluid matrix ($\alpha$) undergoes a budding transformation as soon as the domain size has reached a certain maximal value, which depends on the interplay of spontaneous curvature, bending rigidity, and line tension. The successive stages of the budding process are indicated by (1), (2), and (3). This cartoon was first published in 1992 [34]; similar cartoons have recently appeared in various places [60–64].

For one-component membranes or multi-component membranes with a homogeneous composition, budding can be induced by changes in temperature or osmotic conditions which lead to an increase in vesicle area or a decrease in vesicle volume [58, 59]. In addition, multi-component membranes provide a rather general mechanism for budding via the formation and growth of intramembrane domains as will be described in the next subsection.

Budding involves the formation of a small membrane neck that arises from the shape transformation of a single membrane. There is a rather different process, the fusion of two separate membranes, that leads to the formation of an analogous neck-like membrane structure, now representing the so-called fusion pore. The process of membrane fusion will be discussed in the last subsection.

### *3.1. Domain-induced budding of membranes*

*3.1.1. Budding of single membrane domains.* First, consider a single membrane domain, say $\beta$, which has been nucleated within a membrane matrix, say $\alpha$, and which now grows by diffusion-limited aggregation as shown in figure 8. By definition, an intramembrane domain has a composition which differs from the composition of the membrane matrix. This difference in composition will usually lead to a difference in spontaneous curvature. In addition, the boundary of the domain gives a free energy contribution which is proportional to its length. The corresponding free energy per length defines the line tension $\lambda$. In general, both the spontaneous curvature and the line tension provide a driving force for budding [34, 35].

Even for vanishing spontaneous curvature, a *flat* domain with area $\mathcal{A}_\beta$ and linear size $L \equiv (\mathcal{A}_\beta/\pi)^{1/2}$ does not necessarily represent the state of lowest free energy since the length of the domain boundary can be reduced if the domain forms a bud: the domain boundary now forms the neck of the bud, and this neck narrows down during the budding process; see figure 8. For a membrane domain with bending rigidity $\kappa$ and spontaneous curvature $M_{\rm sp}$, that experiences only a sufficiently small tension, the domain *must* bud as soon as its radius $L$ exceeds a certain maximal size

$$L_{\rm max} = \frac{\kappa}{\lambda}\,\Omega\left(M_{\rm sp}\frac{\kappa}{\lambda}\right) \qquad \text{with } \Omega(x) \approx \Omega_0 \qquad \text{for small } x \tag{4}$$

where $\Omega_0$ is a dimensionless coefficient. The spherical cap model in [34, 35] leads to $\Omega_0 = 8$ whereas a systematic calculation of vesicle shapes [36, 37] leads to $\Omega_0 = 4$. Note that the resulting spherical bud has the radius $R_{\rm bud} \simeq L_{\rm max}/2$.

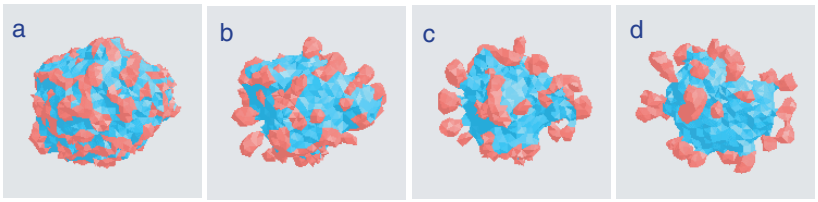


**Figure 9.** Shape sequence of a two-component membrane as observed in Monte Carlo simulations. The vesicle diameter is about 160 nm. The bright and dark patches have zero and finite spontaneous curvature, respectively. (a) Formation and growth of domains; (b), (c) formation of many buds; and (d) coalescence of small buds into larger ones. This shape sequence corresponds to a tensionless membrane. If the vesicle volume is constrained by the osmotic conditions, a tension $\Sigma$ builds up as the buds form and the budding process is truncated when this tension exceeds the boundary value $\Sigma_1$ as given by (5) [49].

It is intuitively clear that the presence of a membrane tension $\Sigma$ acts to suppress the budding process. This effect can be estimated from the spherical cap model which leads to three different tension regimes. Budding without an activation barrier occurs in the low tension regime with [34, 43]

$$\Sigma < \Sigma_1 \equiv \lambda^2/32\kappa \tag{5}$$

where $\lambda$ and $\kappa$ represent the line tension and the bending rigidity as before. As an example, consider the three-component membranes for which domain-induced budding has been observed experimentally [38]. In this case, the line tension was estimated to be of the order of $10^{-10}$, and the low tension regime corresponds to $\Sigma < \Sigma_1 \simeq 10^{-3}$ mJ m$^{-2}$ for a bending rigidity $\kappa \simeq 10^{-19}$ J.

It is important to note, however, that the tension $\Sigma$ is not necessarily constant but will typically increase during the budding process as already pointed out in [34, 35]. For a vesicle, such a tension arises from the constraints on vesicle volume and vesicle area [36, 37]. This is easily understood in the limiting case of conserved vesicle area $4\pi R_{\rm ve}^2$ and conserved vesicle volume $v(4\pi/3)R_{\rm ve}^3$ with volume-to-area ratio $v \leqslant 1$. Thus, assume that the vesicle expels spherical buds of radius $R_{\rm bud}$. Simple geometrical considerations then show that the vesicle can only expel a maximal number $N_{\rm bud}$ of such buds with

$$N_{\rm bud} \approx (1 - v^{2/3})(R_{\rm ve}/R_{\rm bud})^2 \tag{6}$$

as the volume-to-area ratio $v$ approaches one. From an experimental point of view, the simplest way to decrease $v$ is via deflation [37, 43].

Another limiting case is shown in figure 9 for a vesicle without any volume constraint. In this case, each $\beta$ domain that has reached the critical domain size $L_{\rm max}$ as given by (4) can transform into a bud without inducing an effective tension on the remaining $\beta$ domains.

Recently, the cooperative effects of many buds have also been addressed theoretically in the context of caveolae formation [65]. However, in this latter work, the buds are considered as 'inclusions' or point-like defects which ignores the essential processes of domain growth and domain-induced budding. Thus, a systematic theory that determines the membrane tension arising from the formation of many buds remains to be developed.

*3.1.2. Membrane necks and Gaussian curvature.* For a vesicle with a homogeneous (or uniform) composition, the integral over the Gaussian curvature is a topological invariant as shown by the Gauss–Bonnet theorem. This implies that, in the absence of topological changes,

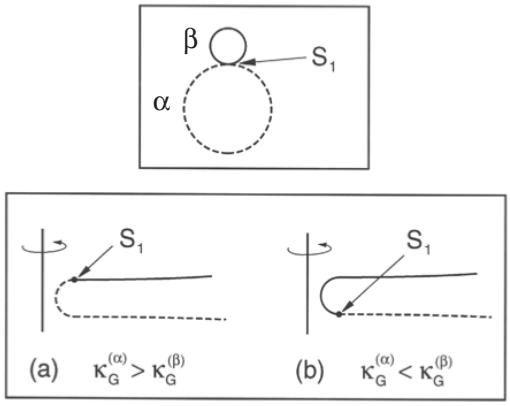


**Figure 10.** Top: side view of a vesicle that consists of a large $\alpha$ domain and a small $\beta$ bud. The two domains are connected by a small neck which contains the $\alpha\beta$ domain boundary. The position of this latter boundary is denoted by $S_1$. Bottom: detailed view of the neck region which shows that the domain boundary position depends on the relative size of the Gaussian curvature moduli $\kappa_G^{(\alpha)}$ and $\kappa_G^{(\beta)}$ of the $\alpha$ and $\beta$ domains. In both cases (a) and (b), the domain boundary is shifted out of the neck towards the domain with the smaller $\kappa_G$, and the neck is now formed by the domain with the larger $\kappa_G$ [37].

the vesicle shape is not affected by this type of curvature and the associated elastic parameter, the Gaussian bending modulus [66].

For a multi-domain membrane, on the other hand, the Gaussian bending modulus will, in general, depend on the membrane composition and, thus, should have different values $\kappa_G^{(\alpha)}$ and $\kappa_G^{(\beta)}$ for the $\alpha$ and $\beta$ domains. It turns out that the difference between these two moduli has an important effect on the structure of the membrane neck between the bud and the mother vesicle [37].

If the difference $|\kappa_G^{(\alpha)} - \kappa_G^{(\beta)}| \ll \kappa$, the domain boundary prefers to sit in the neck in order to minimize its length. Adjacent to the neck region, the mean curvature $M^\beta$ of the bud and the mean curvature $M^\alpha$ of the mother vesicle satisfy the condition [36, 37]

$$\kappa^\alpha (M^\alpha - M^\alpha_{sp}) + \kappa^\beta (M^\beta - M^\beta_{sp}) = \lambda/2 \tag{7}$$

where the bending rigidities $\kappa^\alpha$ and $\kappa^\beta$, and the spontaneous mean curvatures $M^\alpha_{sp}$ and $M^\beta_{sp}$ of the $\alpha$ and $\beta$ domains may, in general, be different.

On the other hand, if the difference $|\kappa_G^{(\alpha)} - \kappa_G^{(\beta)}|$ between the two Gaussian curvature moduli is not small compared to $\kappa$, the domain boundary is moved out of the neck. As shown in figure 10, this domain boundary is shifted towards the membrane domain with the smaller Gaussian bending modulus [36, 37]. In this way, the membrane neck is now formed by the membrane domain with the larger Gaussian bending modulus[3].

*3.1.3. Experiments and simulations of domain-induced budding.* The process of domain-induced budding as described above has recently been confirmed experimentally by optical microscopy of giant vesicles [38, 67, 68].[4] The membranes of these vesicles were composed

[3] In the main text of [37], the description of figure 10 contains two misprints as pointed out by Tobias Baumgart to one of us (RL).

[4] The authors of the recent experimental study in [67] refer to our theory but erroneously state that this theory were restricted to zero spontaneous curvatures of the membrane domains. However, our theory has been developed for general spontaneous curvatures and, thus, also predicts on which side of the membrane the buds are formed.

of the phospholipid DOPC, cholesterol, and sphingomyelin corresponding to the 'raft' mixture that has been postulated to lead to lipid domains in biomembranes [39–41]. For these membranes, the formation of large intramembrane domains was first observed in [42] but these domains showed no tendency to bud, presumably because these vesicles were inflated and under tension. In addition, we had previously observed budding processes for the same membrane composition but have not been able to resolve the associated membrane domains [43]. The experimental observations in [68] show that the domain boundaries are slightly shifted out of the bud necks. This implies that the Gaussian curvature moduli in the two membrane domains are sufficiently different as in figure 10.

The lipid mixture studied in [38, 67, 68] exhibits several coexistence regions and a line of critical points at which the line tension of the domain boundaries must vanish [34]. Close to these critical points, one expects to observe molecular segregation induced by curvature [69] which is, in some sense, opposite to domain-induced budding. This curvature-induced phase segregation is also observed experimentally in [38] when a highly curved vesicle is quenched from the one-phase region towards a critical point.

In view of the recent experiments, it is rather likely that domain-induced budding of giant vesicles has been seen for many other kinds of multi-component membranes [44–48] even though the detection of the underlying membrane domains remains an experimental challenge. The same process also occurs for smaller vesicles that have a diameter of 20–200 nm as observed in different kinds of computer simulations [49–52], compare figure 9.

### *3.2. Fusion of membranes*

Membrane fusion is a ubiquitous process of life. A prominent example is provided by the fusion of synaptic vesicles to the outer membranes of nerve cells. This fusion process is responsible for the release of neurotransmitters into the synaptic cleft and, thus, for the communication between these cells. In this way, membrane fusion provides the molecular basis for all our thoughts. Another less pleasant example is viral infection. Many viruses such as the influenza or the HIV virus hide behind a membrane that they have 'stolen' from an infected cell. They then 'misuse' this membrane and fuse it with the outer membrane of another cell which becomes infected as well. In addition, we find many more fusion processes when we look at the heavy membrane traffic that is present in *all* cells of our body. Indeed, each of these cells contains a huge number of vesicles and other membrane bound compartments (organelles). Many of these vesicles act as transport vehicles that shuttle between the different intracellular compartments and deliver their cargo via membrane fusion.

In spite of its ubiquity, the mechanisms that govern the process of membrane fusion are still poorly understood. There are several reasons for this. First, membrane fusion involves a wide range of length scales: it starts with the formation of the fusion pore on the nanometre scale and proceeds with the opening of this pore in order to release and mix the volumes of the membrane compartments. Second, it also involves a wide range of timescales. In fact, there is a large experimental uncertainty about the different timescales involved in the fusion process. The formation of the fusion pore takes presumably less than 100 $\mu$s as deduced from patch clamp measurements [70]. Furthermore, observations of fusion processes by optical microscopy have been limited so far to normal video frequencies, i.e., to tens of milliseconds. Third, the fusion of biomembranes involves different kinds of proteins [71, 72] and lipids which act in a cooperative way that cannot be monitored with the available experimental methods.

As described in the following, we have recently used computer simulations [53] and optical microscopy [54] in order to gain further insight into the length and timescales involved in the multiscale process of membrane fusion.

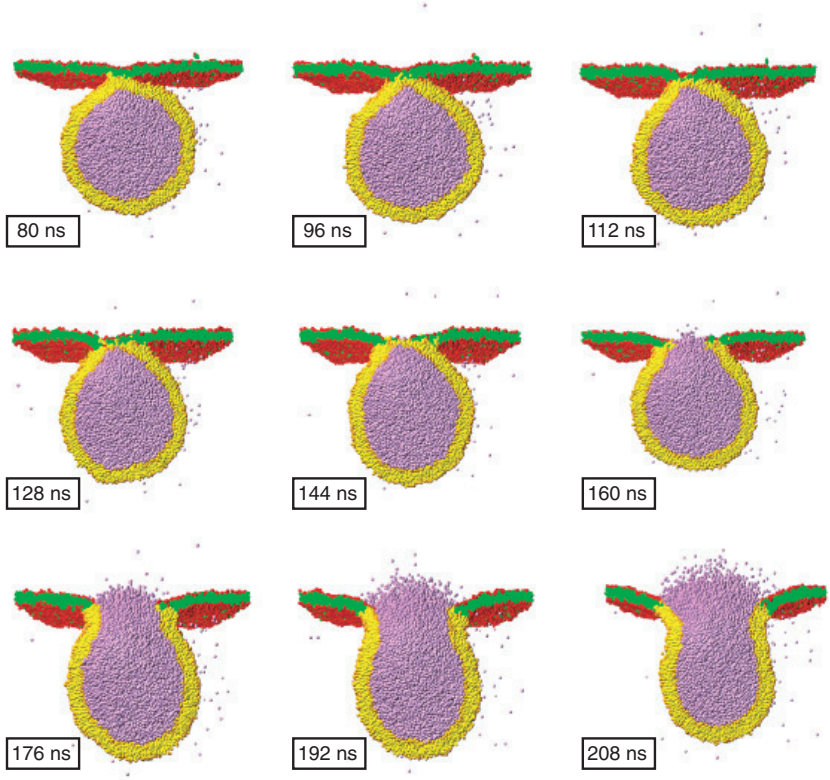


**Figure 11.** Single fusion event of a vesicle (yellow/orange), that has a diameter of 28 nm, with a planar membrane (green/red), that has an area of $50 \times 50$ nm$^2$ square nanometres. The violet particles inside the vesicle represent water molecules; the corresponding particles outside the vesicle are not shown for clarity. The nine snapshots represent the time evolution of the fusion process between 80 and 208 ns. In this example, the fusion pore has been completed after 160 ns [53].

*3.2.1. Simulations: fusion of small vesicles.* Some years ago, we started to simulate the behaviour of bilayer membranes built up from lipid-like molecules. We first used coarse grained molecular dynamics simulations in order to determine membrane states of low tension and to measure the bending rigidity of these membranes from the shape fluctuations [73, 74]. More recently, this approach has been extended to two-component membranes [75]. In addition, a new simulation code based on dissipative particle dynamics (DPD) has been developed by which one can explore larger systems over longer timescales [76].

DPD is a mesoscopic simulation method that explicitly includes water particles, incorporates the correct hydrodynamic forces [77–79], and is capable of simulating millions of molecules. In the context of amphiphilic systems, this method had been previously used to explore the self-assembly and phase behaviour of lipid molecules [80, 76, 81].

Using the DPD technique, we have been able to study the fusion of a lipid vesicle, that has a diameter of 28 nm, with a planar lipid membrane with an area of $50 \times 50$ nm$^2$ within a water volume of $50 \times 50 \times 50$ nm$^3$; see figure 11 [53]. In contrast to previous fusion simulations based on Brownian dynamics [82], coarse grained molecular dynamics [83, 84], and Monte Carlo simulations [85], our study addressed a relatively large number of fusion attempts in order to explore the dependence of the fusion *statistics* on the initial membrane tensions.

The time evolution of one successful fusion event is shown in figure 11. When the simulation starts, the two bilayers of the vesicle and planar membrane are separated by a thin water layer of 1.5 nm. After about 80 ns, the membranes have been brought into contact by Brownian motion. During the next 60 ns, the lipid molecules within the contact zone are rearranged in such a way that the two membranes undergo hemifusion, i.e., the two bilayers have merged into a single one. This molecular intermingling process seems to represent a new fusion step which has not been reported previously. The resulting hemifused state is rather short lived and ruptures relatively quickly. This latter step leads to a complete fusion pore that connects the two membranes in a smooth neck-like fashion. The water within the vesicle can then flow through the fusion pore and, in this way, is released from the vesicle compartment.

One important insight provided by these simulations is that the fusion process can be controlled by the initial tensions within the two membranes. For each membrane, this tension depends on the ratio of the membrane area and the number of assembled lipid molecules. The membrane is tensionless or 'relaxed' when each lipid molecule has a certain optimal area but becomes 'tense' for larger areas per lipid molecule.

No fusion is observed, within a couple of microseconds, when vesicle and planar membrane are initially 'relaxed'. Instead, the vesicle adheres to and spreads onto the planar membrane. If the vesicle membrane is too 'tense' initially, it ruptures before fusion with the second membrane can occur. Likewise, a large initial tension within the planar membrane leads to premature rupture of this latter membrane. As a consequence, fusion can only occur at intermediate values of the membrane tensions. However, even for intermediate tensions, only about 55% of all fusion attempts lead to successful fusion events. In the other cases, the membranes rupture or attain a stable hemifused state.

Each successful fusion event can be characterized by its fusion time, i.e., by the time from first membrane contact to the appearance of a complete fusion pore. This time represents a random variable since it differs from fusion event to fusion event even if the initial membrane tensions are the same. The corresponding histograms have two remarkable features. First, the fusion time distributions for different tensions have significant overlap and are all centred between 200 and 300 ns. Second, no fusion event has been observed with a fusion time between 350 ns and 2 $\mu$s. This cut-off in the fusion time distribution is related to the stabilization of hemifused membranes at lower tension values. This cut-off time is expected to have a similar size for the tension-induced fusion of two vesicles that have a similar size, but should be shifted towards larger values if one considers the fusion of membranes that are rather different in size.

These simulations can be extended in several ways. First, we want to improve the membrane modelling in such a way that the tension of rupture assumes more realistic values for lipid bilayers. One promising method in this direction is to systematically match the parameters of the coarse grained DPD model with more microscopic models [86, 87]. Second, we want to study the fusion of multi-component membranes to supplement the fusion experiments described in the next subsection. Third, one may also include fusion proteins in the simulations. It is generally believed that the latter fusion processes are based on conformational changes of these proteins which exert localized tensions and bending moments onto the membranes. In general, different fusion proteins should lead to different force patterns acting on the membranes. Such localized force patterns can be included in the computer models and have been found to induce membrane fusion as well. In fact, using localized force patterns, the fusion process is still characterized by a fusion time in the order of 200 ns but this process is now more reliable and less random, an obvious advantage for biological fusion processes.

*3.2.2. Experiments: fusion of giant vesicles.* Finally, let us briefly describe recent experiments on the fusion of giant vesicles as observed by optical microscopy [54]. The

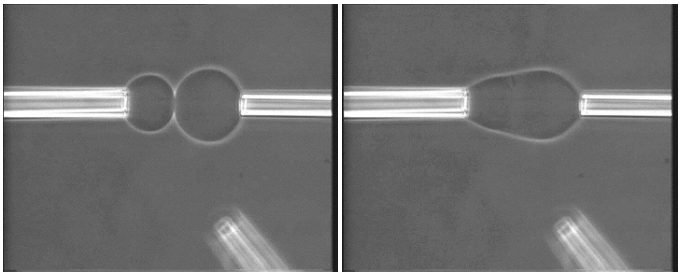

**Figure 12.** Fusion of two lipid vesicles that are aspirated by two (horizontal) micropipettes. The third pipette, which is visible in the lower part of the images, is used to inject small amounts of europium chloride solutions. Left: before the injection, the two vesicles are brought into contact by the micropipettes but do not adhere. Right: after the injection, the two vesicles have fused to form one large compartment.

giant vesicles are bounded by lipid membranes composed of egg phosphotidyl choline (or lecithin) and a small fraction (<0.05 molar per cent) of synthetic lipid-anchored molecules containing a $\beta$-diketonate group [88]. This ligand group is known to form a coordination complex with europium (III) ions with a ligand-to-ion ratio of 2:1. The giant vesicles are prepared by the electroformation method [89]. Using micropipettes with an internal diameter of 5–10 $\mu$m, two vesicles are selected and brought into contact; see the left image of figure 12.

An important improvement of the experimental set-up consists in the possibility to introduce a third pipette into the measuring chamber. With the help of this third pipette that has an internal diameter of about 2 $\mu$m, a small volume of $EuCl_3$ can be locally injected into the contact zone between the two aspirated vesicles. In the absence of the lipid-anchored ligands, the europium ions are adsorbed onto the membranes and induce some tension that leads to membrane rupture at high concentrations. In the presence of the lipid-anchored ligands, the addition of the europium ions leads to fusion of the two adjacent vesicles; see the right image of figure 12. This fusion process seems to be triggered by the cross-linking of ligand groups, which are anchored in different bilayer membranes, by the europium ions. Some fusion events have been observed with high temporal resolution using a fast digital camera with 20 000 frames $s^{-1}$.

## References


[1] Lenz P and Lipowsky R 1998 *Phys. Rev. Lett.* **80** 1920
[2] Gau H, Herminghaus S, Lenz P and Lipowsky R 1999 *Science* **283** 46
[3] Brinkmann M and Lipowsky R 2002 *J. Appl. Phys.* **92** 4296
[4] Kataoka D and Troian S 1999 *Nature* **402** 794
[5] Silver J, Mi Z H, Takamoto K, Bungay P, Brown J and Powell A 1999 *J. Colloid Interface Sci.* **219** 81
[6] Lenz P, Fenzl W and Lipowsky R 2001 *Europhys. Lett.* **53** 618
[7] Gleiche M, Chi L and Fuchs H 2000 *Nature* **403** 173
[8] Lenz P, Bechinger C, Schäfle C, Leiderer P and Lipowsky R 2001 *Langmuir* **17** 7814
[9] Léopoldes J, Dupuis A, Bucknall D and Yeomans J 2003 *Langmuir* **19** 9818
[10] Feng L, Yang Z, Zhai J, Song Y, Liu B, Ma Y, Yang Z, Jiang L and Zhu D 2003 *Angew. Chem. Int. Edn* **42** 4217
[11] Wang J Z, Zheng Z H, Li H W, Huck W T S and Sirringhaus H 2004 *Nat. Mater.* **3** 171
[12] Schäfle C, Brinkmann M, Bechinger C, Leiderer P and Lipowsky R 2005 unpublished
[13] Seemann R, Brinkmann M, Kramer E J, Lange F F and Lipowsky R 2005 *Proc. Natl Acad. Sci. USA* **102** 1848
[14] Quilliet C and Berge B 2002 *Europhys. Lett.* **60** 99
[15] Someya T, Dodabalapur A, Gelperin A, Katz H E and Bao Z 2002 *Langmuir* **18** 5299
[16] Mugele F and Herminghaus S 2002 *Appl. Phys. Lett.* **81** 2303

[17] Klingner A and Mugele F 2004 *J. Appl. Phys.* **95** 2918
[18] Möller G, Harke M and Motschmann H 1998 *Langmuir* **14** 4955
[19] Abbott S, Ralston J, Reynolds G and Hayes R 1999 *Langmuir* **15** 8923
[20] de Crevoisier G, Fabre P, Corpart J-M and Leibler L 1999 *Science* **285** 1246
[21] Ichimura K, Oh S-K and Nakagawa M 2000 *Science* **288** 1624
[22] Lahann H, Mitragotri S, Tran T-N, Kaido H, Sundaram J, Choi I S, Hoffer S, Somorjai G A and Langer R 2003 *Science* **299** 371
[23] Swain P and Lipowsky R 1998 *Langmuir* **14** 6772
[24] Lipowsky R, Lenz P and Swain P 2000 *Colloids Surf.* A **161** 3
[25] Brinkmann M, Kierfeld J and Lipowsky R 2005 *J. Phys.: Condens. Matter* **17** 2349
[26] Rosso R, Verani M and Virga E 2003 *J. Phys. A: Math. Gen.* **36** 12475
[27] Brinkmann M, Kierfeld J and Lipowsky R 2004 *J. Phys. A: Math. Gen.* **37** 11547
[28] Swain P and Lipowsky R 2000 *Europhys. Lett.* **49** 203
[29] Valencia A, Brinkmann M and Lipowsky R 2001 *Langmuir* **17** 3390
[30] Overduin S and Patey G 2003 *J. Chem. Phys.* **119** 8676
[31] Valencia A and Lipowsky R 2004 *Langmuir* **20** 1986
[32] Bernard A-L, Guedeau-Boudeville M-A, Sandre O, Palacin S, di Meglio J-M and Jullien L 2000 *Langmuir* **16** 6801
[33] Lipowsky R, Brinkmann M, Dimova R, Franke T, Kierfeld J and Zhang X 2005 *J. Phys.: Condens. Matter* **17** S537
[34] Lipowsky R 1992 *J. Physique* II **2** 1825
[35] Lipowsky R 1993 *Biophys. J.* **64** 1133
[36] Jülicher F and Lipowsky R 1993 *Phys. Rev. Lett.* **70** 2964
[37] Jülicher F and Lipowsky R 1996 *Phys. Rev.* E **53** 2670
[38] Baumgart T, Hess S and Webb W W 2003 *Nature* **425** 821
[39] Simons K and Ikonen E 1997 *Nature* **387** 569
[40] Mukherjee S and Maxfield F 2004 *Annu. Rev. Cell Dev. Biol.* **20** 839
[41] Schuck S and Simons K 2004 *J. Cell Sci.* **117** 5955
[42] Dietrich C, Bagatolli L A, Volovyk Z N, Thompson N L, Levi M, Jacobson K and Gratton E 2001 *Biophys. J.* **80** 1417
[43] Lipowsky R and Dimova R 2003 *J. Phys.: Condens. Matter* **15** S31
[44] Döbereiner H-G, Käs J, Noppl D, Sprenger I and Sackmann E 1993 *Biophys. J.* **65** 1396
[45] Bradley A J, Maurer-Spurej E, Brooks D E and Devine D V 1999 *Biochemistry* **38** 8112
[46] Holopainen J M, Angelova M I and Kinnunen P K J 2000 *Biophys. J.* **78** 830
[47] Tsafrir I, Caspi Y, Guedeau-Boudeville M-A, Arzi T and Stavans J 2003 *Phys. Rev. Lett.* **91** 138102
[48] Staneva G, Angelova M and Koumanov K 2004 *Chem. Phys. Lipids* **129** 53
[49] Kumar S, Gompper G and Lipowsky R 2001 *Phys. Rev. Lett.* **86** 3911
[50] Kohyama T, Kroll D and Gompper G 2003 *Phys. Rev.* E **68** 061905
[51] Yamamoto S and Hyodo S-A 2003 *J. Chem. Phys.* **118** 7937
[52] Laradji M and Kumar P S 2004 *Phys. Rev. Lett.* **93** 198105
[53] Shillcock J and Lipowsky R 2005 *Nat. Mater.* **4** 225
[54] Haluska C, Marchi-Artzner V, Brienne J, Lehn L M, Lipowsky R and Dimova R 2004 *Biophys. J.* **86** 519A
[55] Buehrle J, Herminghaus S and Mugele F 2003 *Langmuir* **18** 9771
[56] Iliev S and Pesheva N 2003 *Langmuir* **19** 9923
[57] Seifert U and Lipowsky R 1990 *Phys. Rev.* A **42** 4768
[58] Berndl K, Käs J, Lipowsky R, Sackmann E and Seifert U 1990 *Europhys. Lett.* **13** 659
[59] Lipowsky R 1999 *Statistical Mechanics of Biocomplexity* (*Lecture Notes in Physics*) ed D Reguera, J M Rubi and J M B Vilar (Berlin: Springer) pp 1–23
[60] Galbiati F, Razani B and Lisanti M P 2001 *Cell* **106** 403
[61] Shin J-S and Abraham S 2001 *Science* **293** 1447
[62] Nicolas A and Fourcade B 2003 *Eur. Phys. J.* E **10** 355
[63] Degroote S, Wolthoorn J and van Meer G 2004 *Semin. Cell Dev. Biol.* **15** 375
[64] Norris V, Woldringh C and Mileykovskaya E 2004 *FEBS Lett.* **561** 3
[65] Sens P and Turner M 2004 *Biophys. J.* **86** 2049
[66] Helfrich W 1973 *Z. Naturf.* c **28** 693
[67] Bacia K, Schwille P and Kurzchalia T 2005 *Proc. Natl Acad. Sci. USA* **102** 3272
[68] Baumgart T, Das S, Webb W W and Jenkins J T *Preprint*

[69] Seifert U 1993 *Phys. Rev. Lett.* **70** 1335
[70] Lindau M and de Toledo G 2003 *Biochim. Biophys. Acta* **1641** 167
[71] Jahn R and Grubmüller H 2002 *Curr. Opin. Cell Biol.* **14** 488
[72] Mayer A 2002 *Annu. Rev. Cell. Dev. Biol.* **18** 289
[73] Goetz R and Lipowsky R 1998 *J. Chem. Phys.* **108** 7397
[74] Goetz R, Gompper G and Lipowsky R 1999 *Phys. Rev. Lett.* **82** 221
[75] Imparato A, Shillcock J and Lipowsky R 2004 *Europhys. Lett.* **69** 650
[76] Shillcock J C and Lipowsky R 2002 *J. Chem. Phys.* **117** 5048
[77] Hoogerbrugge P J and Koelman J M V A 1992 *Europhys. Lett.* **19** 155
[78] Groot R and Warren P 1997 *J. Chem. Phys.* **107** 4423
[79] Vattulainen I, Karttunen K, Besold G and Polson J 2002 *J. Chem. Phys.* **116** 3967
[80] Yamamoto S, Maruyama Y and Hyodo S-A 2002 *J. Chem. Phys.* **116** 5842
[81] Kranenburg M, Venturoli M and Smit B 2003 *Phys. Rev.* E **67** 060901
[82] Noguchi H and Takasu M 2001 *J. Chem. Phys.* **115** 9547
[83] Marrink S and Mark A 2003 *J. Am. Chem. Soc.* **125** 11144
[84] Stevens M, Hoh J and Woolf T 2003 *Phys. Rev. Lett.* **91** 188102
[85] Müller M, Katsov K and Schick M 2003 *Biophys. J.* **85** 1611
[86] Nielsen S, Lopez C, Srinivas G and Klein M 2004 *J. Phys.: Condens. Matter* **16** R481
[87] Ortiz V, Nielsen S, Discher D, Klein M, Lipowsky R and Shillcock J 2005 *J. Phys. Chem.* B submitted
[88] Richard M-A, Marchi–Artzner V, Lalloz M-N, Brienne M-J, Artzner F, Gulik T, Guedeau-Boudeville M-A and Lehn J-M 2004 *Proc. Natl Acad. Sci. USA* **101** 15279
[89] Angelova M and Dimitrov D 1986 *Faraday Discuss. Chem. Soc.* **81** 303